Modelling of Two-Phase Nano Fluid and Steel-Slag Jets

IVAN KAZACHKOV
Nizhyn Gogol State University,
16600 Grafska str.2 Nizhyn,
UKRAINE

Abstract: - The original multiphase method with the introduction of a phase indicator function is applied for mathematical modelling and computer simulation of the mixing and heat transfer processes in the two-fluid turbulent heterogeneous jets. Differential equations for the axially symmetrical two-dimensional stationary flow and the integral correlations in a cylindrical coordinate system are considered for the jet of fluid from a nozzle into a space filled with another fluid that is not miscible with the first one. Parameters of the turbulent mixing during the spreading of such jets are modeled and analyzed. For computer simulation, the FLEX PDE platform is implemented. The method proved successfully during the half of the century in many different physical tasks, including experimental studies using the invented two-phase micro-sensor. The results obtained for the turbulent flow of a few nanofluids and Steel-slag jets are important for research and industrial tasks, where the calculation of multiphase turbulent mixing and heat transfer gives precise detail characteristics of the heat and mass transfer processes.

Key-Words: - Turbulent, Two-Phase, Jets, Mixing, Immiscible, Function-indicator, Nanofluid, Computer Simulation.

Received: March 9, 2026. Revised: April 22, 2026. Accepted: May 17, 2026. Published: September 15, 2026.

1 Introduction

Additive manufacturing (AM), also known as 3D printing, has many advantages, including the elimination of special tooling, flexible and customizable design, and efficient usage of raw materials. Binder jetting is one of the seven AM technologies defined by ASTM and ISO, [1].

When binder jetting is used to fabricate a part, a powder bed is first formed, then a green part is created by selectively jetting a liquid binder onto the powder bed, and finally the green part is densitified by sintering [1]. Advantages of binder jetting include complimentary support and ease of debinding, [2], [3].

The feedstock powders used in binder jetting include nanopowder (or submicron powder), [4], [5], [6], [7], micropowder [8], [9], [10], [11], [12], [13], [14], and granulated powder [7], [15], [16], [17], [18], [19], [20], [21], [22], [23]. Granulated powder is often prepared from nanopowder, and the granule size is usually in the micrometer range, [21], [22], [23].

Alumina nanopowder (90-187085) was acquired from Allied High Tech, USA. Alumina micropowder (26R-8S70) was acquired from Inframat, USA. Spray freeze drying [7], [22] was chosen as the granulation method in this study. A slurry with a solid loading of 20 vol.% was prepared from the nanopowder described above.

The preparation started with adding water and alumina milling balls into a high-density polyethylene bottle with a capacity of 1000 mL. Some parameters of the materials are given below [24]:

Apparent density and tap density of three powders

Absolute apparent density and tap density (g/cm^3)

Nanopowder 0.29±0.001 0.55±0.012

Micropowder 2.09±0.004 2.38±0.019

Granulated powder 0.46±0.006 0.56±0.007

Water, Alumina Nano powder and micro powder considered in the paper are as follows:

1 Alumina Nano powder is flowing from the nozzle into the space of water ρ_{21}=0.55/1=0.55.

2 Micro Powder Flows from the Nozzle into the Space of Water ρ_{21}=2.38/1=2.38

Inversely, water is supplied from the nozzle into Nano powder and micro powder: ρ_{21}=1/0.55=1.82, ρ_{21}=1/2.38=0.42.

True density: This relates to the ratio of the mass and the volume (true volume) of a sample, excluding the volume of the open pores, the closed pores, and the inter-particle voids. Skeletal density: This is the ratio of the mass to the volume (skeletal volume) of the particles, excluding both inter-particle voids and opened pores.

Tapped density: This is the density measured by mechanically tapping a container of particles to create a regular vibration, which rearranges the powder particles. The measurement of tapped density is typically conducted using a tapped density tester.

Bulk density: This is the density measured after the particles have freely filled a standard container under specific conditions, i.e., the mass of the particles per unit volume when they are loosely packed, [25].

2 The Method for Modeling of Multiphase Turbulent Flows

Parameters (density of liquid, flow velocity, temperature, etc.) of a mixture in the turbulent multiphase flow are considered in accordance with the method [26], developed and reported in many publications, e.g., [27], [28]. The analog of the Navier-Stokes equations in a boundary layer approach was derived in the following form [26]:

$$\sum_{i=1}^{m}\left[\frac{\partial}{\partial x}(y\rho_i B_i u_i)+\frac{\partial}{\partial y}(y\rho_i B_i v_i)\right]=0, \quad (1)$$

$$\sum_{i=1}^{m}\rho_i B_i \left(u_i\frac{\partial u_i}{\partial x}+v_i\frac{\partial u_i}{\partial y}\right)=-\frac{dp}{dx}+\frac{1}{y}\frac{\partial}{\partial y}\left[y\sum_{i=1}^{m}B_i\tau_i\right]_m,$$

where $a^l(t)=\sum_{i=1}^{m}B_i(t)a_i^l(t)$, $\sum_{i=1}^{m}B_i=1$.

The function-indicator $B_i(t)$ is introduced for the phases in multiphase flow as follows:

$$B_i(t)=\begin{cases}1, & i-\text{phase occupies elementary volume } \delta V\\ 0, & i-\text{phase is outside elementary volume } \delta V\end{cases}$$

In the stationary equations (1) for the flow of incompressible liquids, written in a cylindrical coordinate system, are: p- pressure, ρ- density, u,v- the longitudinal and transversal velocity components, τ_i- turbulent stress for the i-phase. All parameters of the flow are averaged on the characteristic interval by time chosen. Index m belongs to the values at the axis of the flow (symmetry axis).

The function-indicator of a phase in multiphase flow is considered as the mathematical expectation, in contrast to the other multiphase approaches [8], [9], [10], which are based on the introduction of the volumetric specific content of a phase in multiphase flow. The function-indicator allows computing the volumetric specific content of the phases. Development of the model for a two-phase jet corresponds to the Figure 1 and schematic representation is shown in Figure 2, where r_0 – radius of a nozzle, u_{01}- velocity at the nozzle. The conical surface 1 in Figure 1 is a boundary of a homogeneous potential core a, the internal sublayer b_1 contains an ejected liquid as a disperse phase, while the external sublayer b_2 contains the liquid outgoing from the nozzle as a disperse phase.

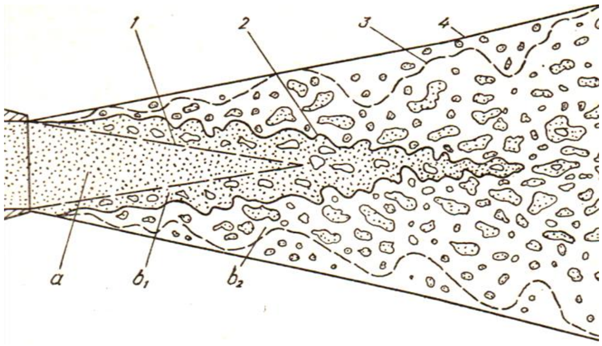

Fig. 1: General view of multiphase turbulent jet
Source: [26].

The internal and external sublayers are divided by the surface of phase inverse 2; and the surface 3 is dividing the turbulent and laminar flow zones 3, which is the most indefinite one; 4 is an external conical surface of the axisymmetric mixing zone (conditionally smooth).

Due to a limited regularity of the processes occurring in turbulent jets, the surfaces 2 and 3 in Figure 1 are blurred into the corresponding regions of inversion and intermittency. The external boundary of the jet is the outer envelope surface 4 of the set of surfaces 3. The uniform velocity profile is assumed for the first liquid going from the nozzle. The surrounding liquid (phase 2) is in the rest before the first liquid starts flowing from the nozzle.

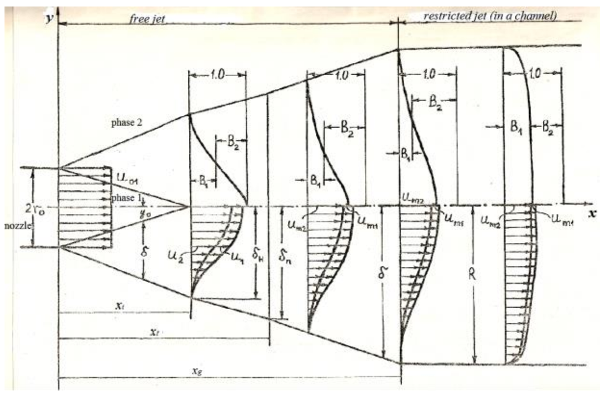

Fig. 2: Schematic representation of multiphase turbulent jet confined by channel at the distance xg
Source: [26].

The structural scheme for the mixing process in Figure 2 is simplified: the initial part of the length x_i with the approximately linear boundaries for the conical surface (in cylindrical coordinate system) of the internal core of a first phase and mixing zone between internal and external boundaries of the jet.

The turbulent zone contains fragments of the phases as far as immiscible liquids have behaviors like the separate phases, with their interfacial multiple surfaces. The first phase in a potential core is totally spent in an initial part of the mixing zone. Then a short transit area follows. Afterwards the ground part of the two-phase jet begins, with the two phases well mixed across the entire layer of a jet.

The external boundary of a mixing zone is determined by zero longitudinal velocity of the second phase and zero transversal velocity of the first phase. The second phase is sucked from an immovable surrounding into a mixing zone.

The function-indicator of the first phase $B_1(t)$ is zero at the external interface because it is absent in the surrounding medium. Similarly, the function-indicator $B_2(t)$ is zero on the boundary of the potential core, the interface of the first phase flowing from the nozzle. In a first approach, the influence of the mass, viscous, and capillary forces are neglected.

With account of the above-mentioned, the boundary conditions are [26]:

$$y=y_0,\ u_i=u_{0i},\ v_i=0,\ \tau_i=0,\ B_1=1,\ \partial B_1/\partial\eta=0;$$

$$y=y_0+\delta,\ u_i=0,\ v_i=0,\ \tau_i=0,\ B_1=0. \qquad (2)$$

And dependence of the function-indicator B_1 from the longitudinal coordinate x is introduced through the second derivative of it at the boundary of a jet $y=y_0$: $\partial^2 B_1/\partial\eta^2 = h(x)$.

2.1 Approximation of Velocity Profiles and Function-Indicator

The turbulent stress in the phase is stated by the "new" Prandtl's formula $\tau_i=\rho_i\,\kappa_i\delta u_{mi}\,\partial u_i/\partial y$, where κ_i is the coefficient of turbulent mixing for the i-th phase, δ is the width of the mixing layer. The polynomial approximations for the velocity profiles and other functions have been obtained based on the boundary conditions (2) [26], [27], e.g.

$$u_1/u_{01} = 1-4\eta^3+3\eta^4, \qquad (3)$$

$$u_2/u_{02} = 1-6\eta^2+8\eta^3-3\eta^4, \qquad (4)$$

$$B_1 = B_1^{(0)} = 1-\eta^3+0.5\eta^2(1-\eta)h(x), \qquad h\in[-6,0],$$

$$B_1 = B_1^{(1)} = 1-4\eta^3+3\eta^4+0.5\eta^2(1-\eta)^2 h(x),$$
$$h\in[-12,-6],$$

$$B_1 = B_1^{(2)} = 1-10\eta^3+15\eta^4-6\eta^5+0.5\eta^2(1-\eta)^3 h(x),$$
$$h\in[-20,-12],$$

$$B_1 = B_1^{(3)} = 1-20\eta^3+45\eta^4-36\eta^5+10\eta^6+0.5\eta^2(1-\eta)^4 h(x),$$
$$h\in[-30,-20], \qquad (5)$$

$\eta=(y-y_0)/\delta$. Function h(x)=$\left(\partial^2 B_1/\partial\eta^2\right)_{\eta=0}$ is responsible for the variation of B_1 by x, it may vary in the range $h\le 0$ due to requirements of its nature.

The first approximation $B_1(\eta)$ in (5) reveals restricted application in the range $h\in[-6,0]$, while outside of this region it does not satisfy the boundary conditions (2) and the condition $0\le B_1(\eta)\le 1$, $\forall\eta\in[0,1]$. Therefore, all the next approximations $B_1(\eta)$ in (5) were obtained as a transition of the piecewise continuous function-indicator $B_1^{(n)}$ to its next approximation following the condition that the derivative by η with respect to a point $\eta=1$ is zero up to (n+1)-th order. These functions have the breaks at the transition points of the permanent characteristic function $B_1^{(n)}(\eta,h)$ from the one regional approximation to the other one (a first derivative has break at those points).

The polynomial approximations for u_2, B_1 remain the same on a ground part of the jet but for the function u_1 the approximation is

$$u_1/u_{m1} = 1-3\eta^2+2\eta^3. \qquad (6)$$

The real profiles for the multiphase flow are represented as a product of the corresponding profile multiplied by its function-indicator.

2.2 The Advantages of Polynomial Profiles

The advantage of such approximations is that all functions $B_1^{(n)}$ are smoothly transforming from one region by h(x) to the next one. Each function $B_1^{(n)}$ exactly coincides with the previous one $B_1^{(n-1)}$ at the conjugation boundary, where the $B_1^{(n-1)}$ ends and the $B_1^{(n)}$ starts.

Physical meaning of the varying approximations $B_1^{(n)}$ is determined by dependence of the phase distribution in the mixing layer on the density ration of the mixing phases: the higher is density of the surrounding liquid, the shorter is penetration of the first, lighter phase, into the mixing layer.

The disadvantage of the above approximations is a growing complexity of the functions $B_1^{(n)}$ in analytical calculation, which is nevertheless easily fought by modern computer analytical calculations. It is impossible to get a common approximation for $B_1(\eta, h)$ satisfying the boundary conditions (2) in all range by parameter i_0 (due to the requirement of variation B_1 from 0 to 1).

3 Equations for the Jet at Initial Part

3.1 The Integral Correlations

Based on (3)-(5), the integral correlations have been derived for the two-phase turbulent jet [26], [27] integrating the mass and momentum conservation equations (1) with the boundary conditions (2) for the total cross-section of a flow $y=y_0+\delta$, as well as the momentum conservation for $y=y^*$, respectively:

$$u_{01}\left(r_0^2-y_0^2\right)=2\delta\int_0^1 B_1u_1\left(y_0+\delta\eta\right)d\eta\,,$$

$$\rho_1u_{01}^2\left(r_0^2-y_0^2\right)=2\delta\int_0^1\left(\rho_1B_1u_1^2+\rho_2B_2u_2^2\right)\left(y_0+\delta\eta\right)d\eta,$$

$$\rho_1u_{01}\left(u_{01}-u_1^*\right)y_0y_0'+\frac{d}{dx}\delta\int_0^{\eta^*}\sum_{j=1}^{2}\rho_jB_ju_j^2\left(y_0+\delta\eta\right)d\eta-$$

$$\sum_{j=1}^{2}u_i^*\frac{d}{dx}\delta\int_0^{\eta^*}\rho_iB_iu_i\left(y_0+\delta\eta\right)d\eta= \qquad (7)$$

$$=\left(y_0+\delta\eta^*\right)\sum_{j=1}^{2}\rho_jB_j\kappa_ju_{0j}\frac{\partial u_j^*}{\partial\eta}, \qquad B_1+B_2=1.$$

The first equation in (7) was got integrating the mass conservation equation by y, the second and the third ones – integrating the momentum conservation for the total flow of a two-phase mixture for $y=y_0+\delta$ and $y=y^*$, respectively. The parameters at $\eta=\eta^*<1$ are signed with a star *.

The equation array (7) for the initial part of the jet is transformed to the following dimensionless form with the scales r_0, δ, u_{0i} for the longitudinal and transversal coordinates and velocity, respectively:

$$y_0^2+2\delta\sum_{j=1}^{2}y_0^{2-j}\delta^{j-1}a_j=1,$$

$$y_0^2+2\delta\sum_{j=1}^{2}y_0^{2-j}\delta^{j-1}\left(a_{j+2}+i_0b_{j+2}\right)=1, \qquad (8)$$

$$\left(1-u_1^*\right)y_0\frac{dy_0}{d\varsigma}+\frac{d}{d\varsigma}\delta\sum_{j=1}^{2}y_0^{2-j}\delta^{j-1}\left(a_{j+2}^*+i_0b_{j+2}^*\right)-$$

$$\frac{d}{d\varsigma}\delta\sum_{j=1}^{2}y_0^{2-j}\delta^{j-1}\left(a_j^*u_1^*+i_0b_j^*u_2^*\right)=$$

$$=\left(y_0+\delta\eta^*\right)\sum_{j=1}^{2}B_j^*\left(\frac{\partial u_j}{\partial\eta}\right)^*\left(i_0\kappa_{21}\right)^{j-1}.$$

Here are: $\bar{y}_0=y_0/r_0$, $\bar{\delta}=\delta/r_0$, $\eta=\left(y-y_0\right)/\delta$, $\bar{x}=x/r_0$, $\varsigma=\kappa_1\bar{x}$, $s_0=u_{02}/u_{01}$, $i_0=ns_0^2$,

$$n=\rho_2/\rho_1,\ \kappa_{21}=\kappa_2/\kappa_1,\ a_i=a_{i1}+a_{i2}h,$$

$$b_i=b_{i1}+b_{i2}h,\quad a_i=\int_0^1 B_1\bar{u}_1\eta^{j-1}d\eta,$$

$$b_i=\int_0^1 B_2\bar{u}_2\eta^{j-1}d\eta \text{ (i=1, 2)};\ a_i=\int_0^1 B_1\bar{u}_1^2\eta^{j-1}d\eta,$$

$$b_i=\int_0^1 B_2\bar{u}_2^2\eta^{j-1}d\eta \text{ (i=3, 4); j=1, 2.}$$

The computed values of the integral parameters in (8) have been obtained in a range of variation of the function h(x) according to the approximation of the velocity profiles (3), (4), and the function-indicator of the phase B_1 (5). As shown below mostly the region by parameter h(x) is covered in (5) for the bright enough density ratio of the mixing liquid phases.

The coefficients a_{ij}, b_{ij} are computed according to the introduced profiles. The integral correlation for the part of the mixing layer in the system (8) are taken by $\eta=0.5$. The corresponding coefficients a_{ij}^*, b_{ij}^* are computed for this middle section of the mixing layer, [26], [27].

3.2 Dimensionless Boundary Problem

Except the above, for the dimensionless parameters we retain the same notations as for the dimensional ones. Only here in (8) it is stated for clarification of the dimensionless notations.

The sliding factor s_0 is supposed to be constant. Boundary conditions (2) for (8) are transformed as

$$\zeta=0,\ y_0=1,\ \delta=0;\qquad \zeta=\zeta_i,\ y_0=0,\ \delta=\delta_i; \qquad (9)$$

where ζ_i, δ_i are the dimensionless length of a jet and its maximal radius (at the end of the initial part).

The characteristics $y_0(\zeta)$, $\delta(\zeta)$, $h(\zeta)$ are computed from (8), (9). Then all others are got for the stated values of the main parameters: i_0, κ_1, κ_2. The first parameter is slightly indefinite due to difficulties with estimation of the phases' sliding, while the other two are known from the experimental studies for the specific conditions.

The main problem with validation of the mathematical model against the experimental data is correct estimation of the coefficients of turbulent mixing κ_1, κ_2 in each specific case. But the advantage of the model is the possibility to have all characteristics of a flow together with their belonging to a particular phase through the functions B_1, B_2. Distribution of the transversal velocities, interface interactions, coefficients of the volumetric q and mass ejection g, and kinetic energy e_i for the phases in a flow are computed as follows, [26]:

$$\frac{B_1 v_1}{\kappa_1 u_{01}} = B_1 u_1 \frac{d}{d\varsigma}\left(y_0+\delta\eta\right) - \frac{\frac{d}{d\varsigma}\left(0.5y_0^2 + a_1 y_0\delta + a_2\delta^2\right)}{y_0+\delta\eta}$$

$$q = 2s_0\delta\left(b_1 y_0 + b_2\delta\right), \qquad (10)$$

$$\frac{B_2 v_2}{\kappa_1 u_{02}} = B_2 u_2 \frac{d}{d\varsigma}\left(y_0+\delta\eta\right) - \frac{1}{y_0+\delta\eta}\frac{d}{d\varsigma}\left(b_1 y_0\delta + b_2\delta^2\right)$$

$$e_1 = y_0^2 + 2\int_0^1 B_1\bar{u}_1^3\left(y_0+\delta\eta\right)\delta d\eta,$$

$$e_2 = 2i_0 s_0\int_0^1 B_2\bar{u}_2^3\left(y_0+\delta\eta\right)\delta d\eta.$$

For the short transient part of the jet there is no developed substantiated scheme, therefore it is not under consideration here. The ground part is considered after a short transient part. The method is well elaborated and supported with the experimental data, [26].

4 Computer Simulation

4.1 Solution of Boundary Problem for Initial Part of Jet Flow

Solution of the boundary problem (8) allows obtaining the parameters for the initial part of a jet by the stated values i_0, κ_{21}. Computational experiments revealed the basic features of the flow. Velocity distributions for the phases (u_1, u_2) and function-indicators of the phases (B_1, B_2) are stated, as well as the values of parameters at the cross section of the nozzle.

The system (8) contains two algebraic and one differential equation. From the algebraic equation array the functions $y_0(h)$, $\delta(h)$ are got, and then the differential equation is expressed in a standard form

$$dh/d\zeta = F(h(\zeta), i_0, \kappa_{21}),$$

for the numerical solution. The boundary problem (8), (9) was solved numerically. The results of computer simulation are given below.

4.2 Jets of Water Flowing into Oil ($\rho_{21} \approx 0.8$)

Next, the features of water jets flowing into the space with oil, or salt solution - into fresh water, when the ratio of the density of the ejected liquid to that flowing out of the nozzle is approximately $\rho_{21} \approx 0.8$, are considered.

The results of computer simulation are shown in Figure 3, Figure 4 and Figure 5, from which it can be seen that, unlike the previous one, all functions are smooth here, without features. The presented functions $h(\zeta)$, δ, y_0 are practically identical for two different ratios of the turbulent exchange coefficients κ_{21}: 2 and 0.5.

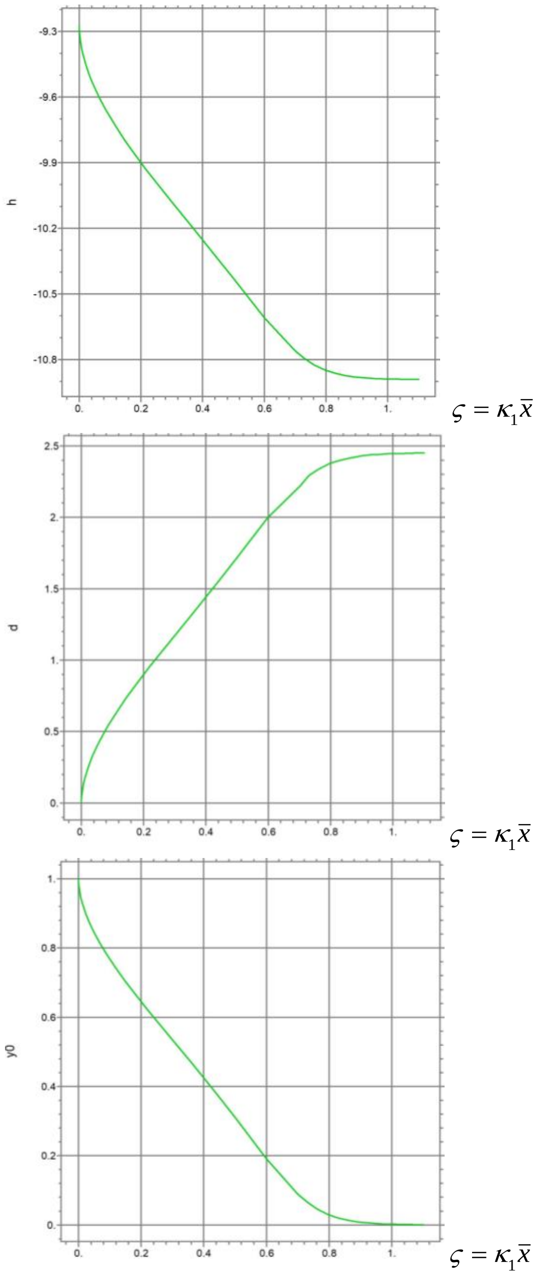

Fig. 3: $h(\zeta)$, width of mixing layer and potential core y0 along axis : i0=0.8, κ21=2δ $\varsigma_i = \kappa_1\bar{x}$

Source: created by the authors.

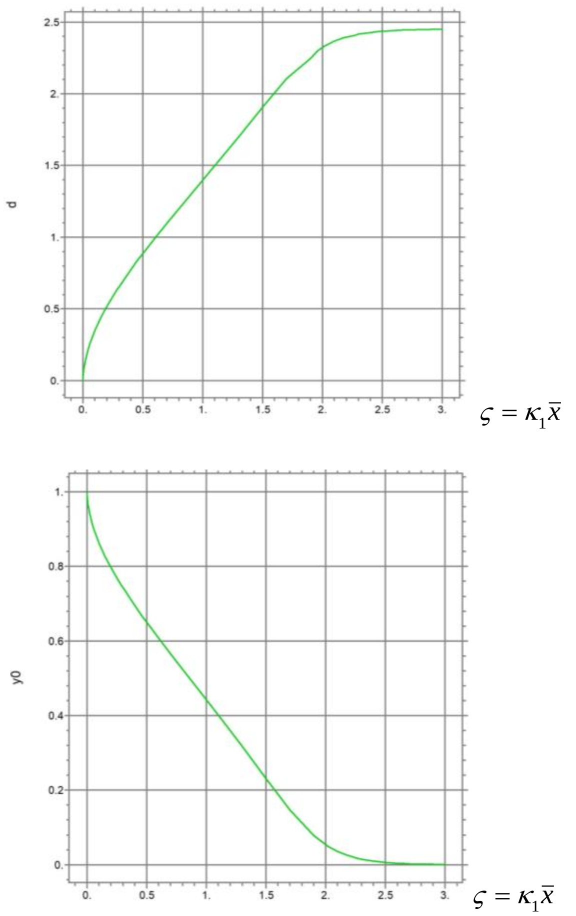

Fig. 4: Widthofmixinglayerδandpotentialcorey0along axis:i0=0.8,κ21=0.5
Source: created by the authors.

Even the values of the width of the mixing region are practically the same and the parameter κ_{21} affects the length of the initial part of the jet: a change from approximately 1.4 to 2.8 (an increase in κ_{21} four times reduces the initial section of the jet by half). The initial section of the jet increases with a decrease in the ratio of the turbulent exchange coefficients.

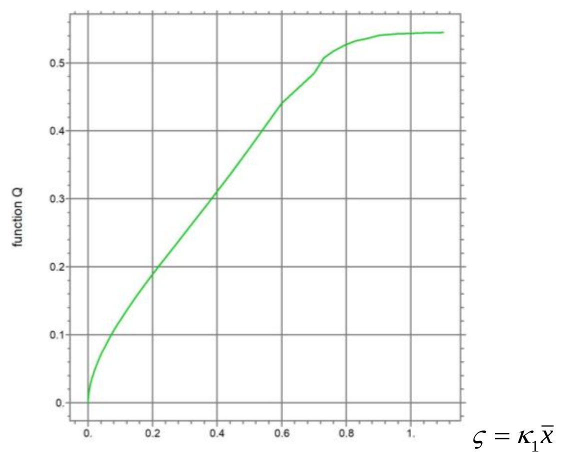

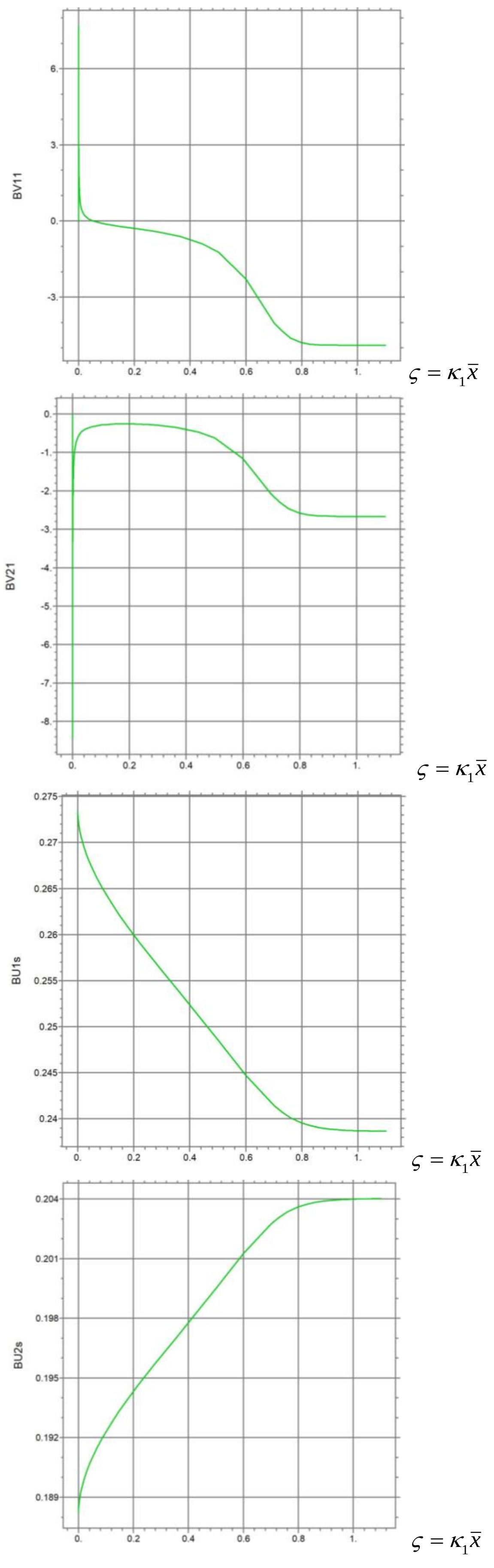

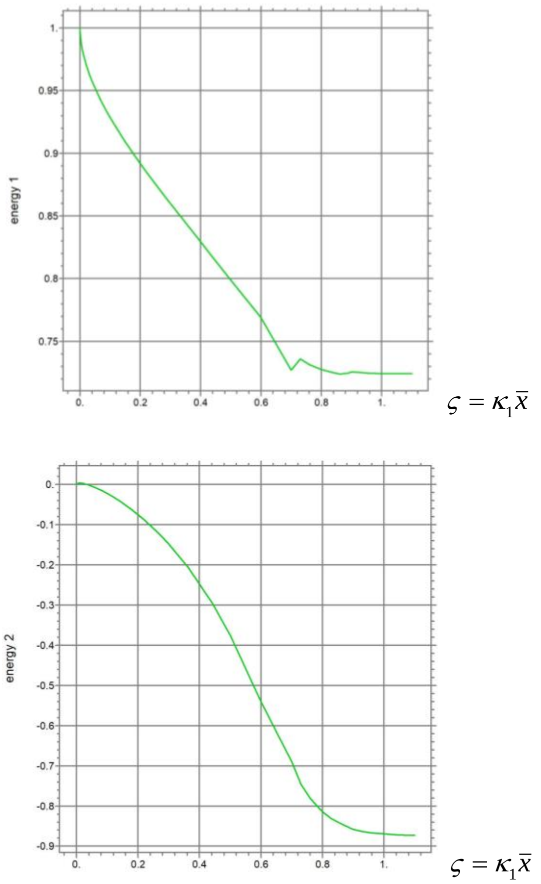

Fig. 5: Velocities of phases inside mixing layer and energy along axis:i0=0.8,κ21=2
Source: created by the authors.

We see in Figure 5 many additional characteristics, which are available only by the applied multiphase method. First the ejection coefficient Q and velocities of the phases at the external boundary of mixing layer along the dimensionless axis $\varsigma = \kappa_1 \bar{x}$ of a jet: a sharp surge in the transverse velocity of the first phase BV_{11} at the nozzle exit towards the stationary liquid of the pool, then a gradual increase in the flow velocity into the mixing region; in the second phase BV_{12}, a sharp injection at the nozzle exit and then a weak one until a constant value is established. BU_{1s}, BU_{2s} show the velocities of the phases in the middle section of the mixing layer.

Finally, the energy of the first phase decreases in the initial part of the jet from 1 to 0.72, and the second phase increases the energy from zero to 0.88. The velocity of the first phase inside the region decreases from 0.274 to 0.238, and the second increases from 0.188 to 0.204. Other characteristics of turbulent mixing in two-phase jet were also calculated by (10). Thus, the method gives unique opportunity for calculation of the detail phase mixing.

4.3 Jet of AL Micro Powder in Water

For this case, density ratio is equal to 2.38. The results of computation are shown in Figure 6: the total expansion of jet reaches about δ=2.1 on a distance $\varsigma = \kappa_1 \bar{x}$ =0.8.

Calculation by different values of the ratio of turbulent mixing coefficients gives the same results here, only the length of the initial part of a jet is shorten with increase of the $\varsigma = \kappa_1 \bar{x}$. All the above detail characteristics we computed too.

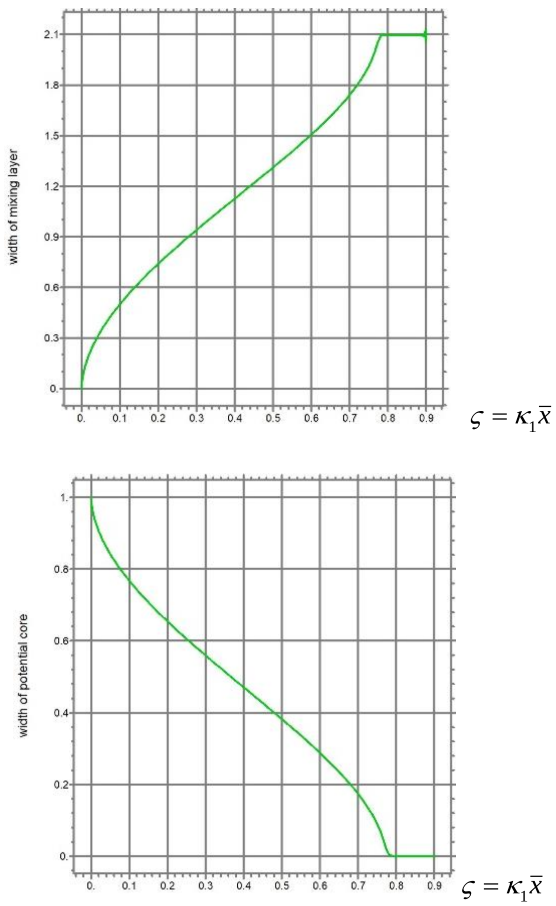

Fig. 6: Width of mixing layer δ and potential core y0 along axis, Al micropowder in water i_0=2.38, κ_{21} =0.5.
Source: created by the authors.

4.4 Jet of Water in AL Micro Powder

Figure 7 presents the results by water jet spreading in a pool of Aluminum powder (i_0=0.42) by the ration of turbulent mixing coefficients κ_{21}=0.5. Here the length of the initial part is $\varsigma = \kappa_1 \bar{x}$ =40 and δ=2.75.

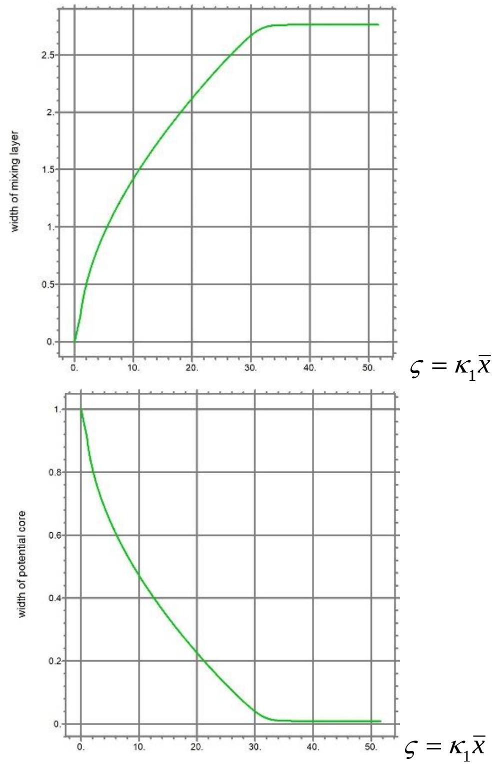

Fig. 7: Water jet in AL micro powder δ(ζ), y_0(ζ) i_0=0.42, κ_{21}=0.5.

Source: created by the authors.

Figure 8 shows the difference of the results by κ_{21}=5:

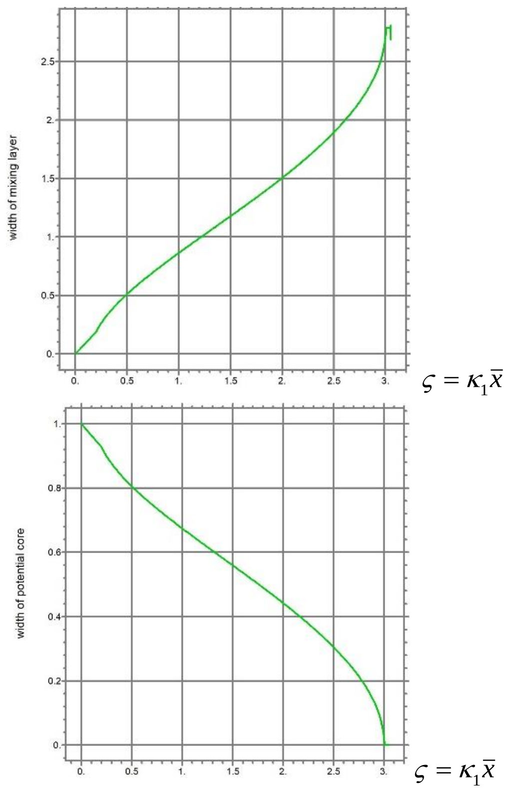

Fig. 8: δ(ζ), y0(ζ) by i0=0.42, =5.0 κ_{21}

Source: created by the authors.

Here the length of the initial part is substantially shorter: $\varsigma = \kappa_1 \bar{x}$ =3. Different is also the character of the functions δ(ζ), y_0(ζ) but the mixing layer is the same.

4.5 Jet of AL Nano Powder in Water

The turbulent jet of AL Nano powder spreading in water was studied with the density ratio as above stated 0.55. The Figure 9 and Figure 10 show the results for varying values of the turbulent mixing coefficients.

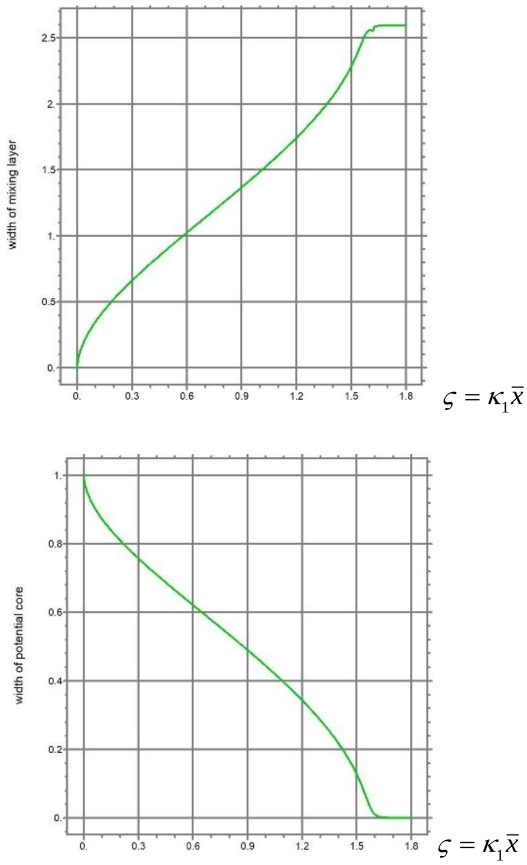

Fig. 9: Jet of a L Nano powder in water:δ(ζ),y0(ζ) byi0=0.55,=0.5

Source: created by the authors.

The width of the mixing layer is 2.6, and the length of the initial part of a jet is $\varsigma = \kappa_1 \bar{x}$ =1.7.

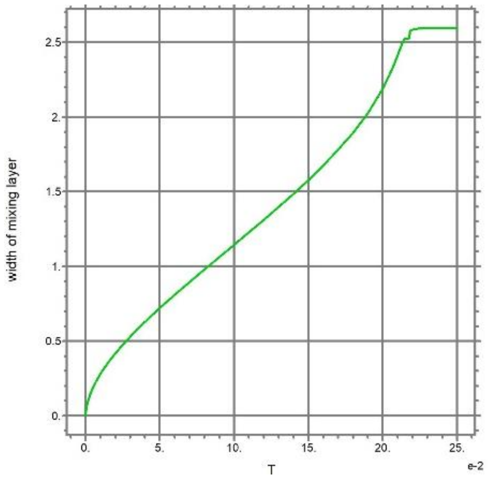

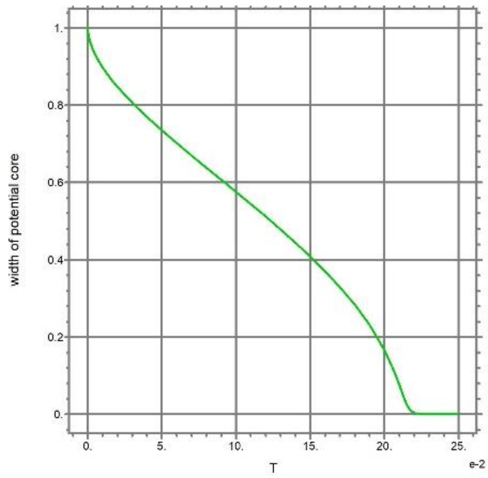

Fig. 10: Jet of a L Nano powder in water:δ(ζ),y0(ζ) byi0=0.55,=5.0

Source: created by the authors.

Despite such a big difference in the ratio of mixing coefficients, similar pictures, only a shorter initial part $\varsigma = \kappa_1 \bar{x}$ =0.25 is observed in Figure 10.

4.6 Jet of Water in AL Nano Powder

The turbulent jet of water spreading in AL Nano powder was studied with the density ratio 1.82. The results are presented in Figure 11.

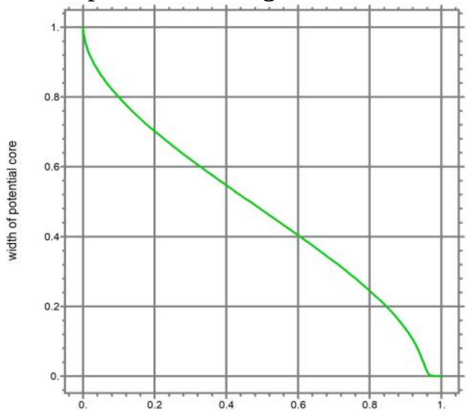

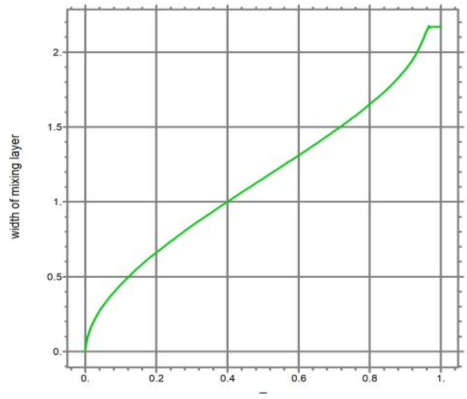

Fig. 11: Jet of water in AL Nano powder δ(ζ), y_0(ζ) by i_0=1.82, κ_{21}=5.0.

Source: created by the authors.

4.7 Steel-Slag Jet Flow

The characteristics y_0(ζ), δ(ζ), h(ζ) are computed from boundary problem (8), (9) with account of (10). Then all others are obtained for the stated values of the main parameters: i_0, κ_1, κ_2. The first parameter is slightly indefinite due to difficulties with estimation of the phases' sliding, while the other two are known from the experimental studies for the specific conditions.

The computer simulations were performed for the steel-slag jet (steel flows from the nozzle into the space with slag), and inversely, for the slag-steel jet (slag jet is going into volume of steel): $i_0 = (\rho_2 / \rho_1) s_0$, ρ_1= 7750, 7900, 8500; ρ_2=2000, 2500, 3000. Thus, i_0=0.258, 0.253, 0.235 (ρ_1= 7750); i_0=0.323, 0.316, 0.294 (ρ_1= 7900); 0.387, 0.380, 0.353 (ρ_1= 8500).

The results are presented in Figure 12, Figure 13, Figure 14, Figure 15, Figure 16 and Figure 17 for i_0=0.235 (ρ_1=8500, ρ_2=2000). Sliding is supposed absent, therefore s_0=1. Actually, phases can slide, sometimes substantially but we have little data about.

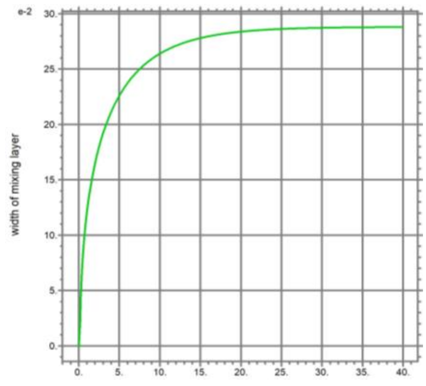

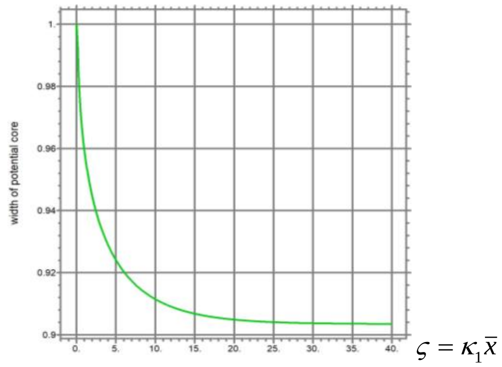

Fig. 12: Functions δ(ζ), y0(ζ) by i0=0.235, κ_{21}=0.5.

Source: created by the authors.

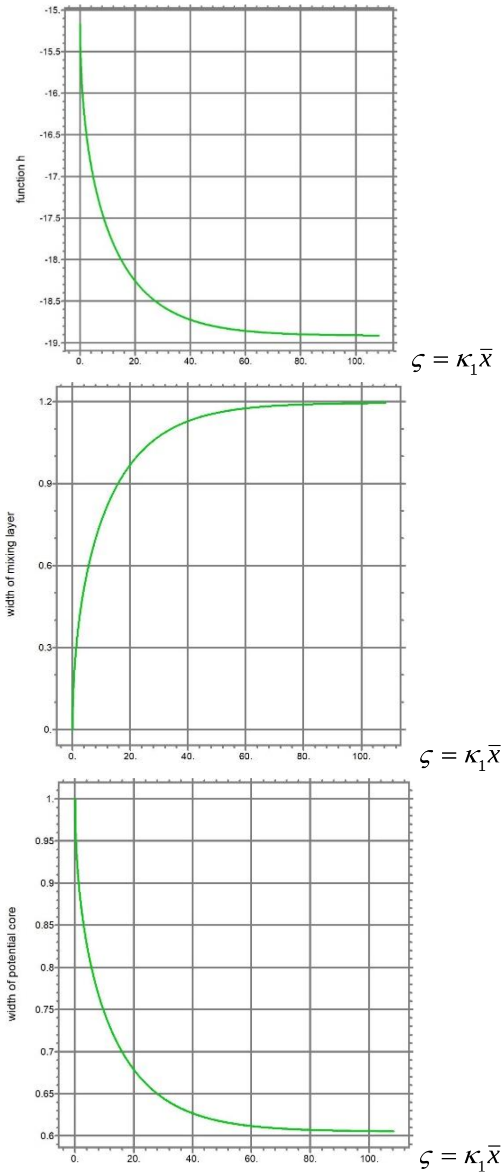

Fig. 13: Functions h(ζ), δ(ζ), y0(ζ) by i0=0.235, κ_{21}=1.0.

Source: created by the authors.

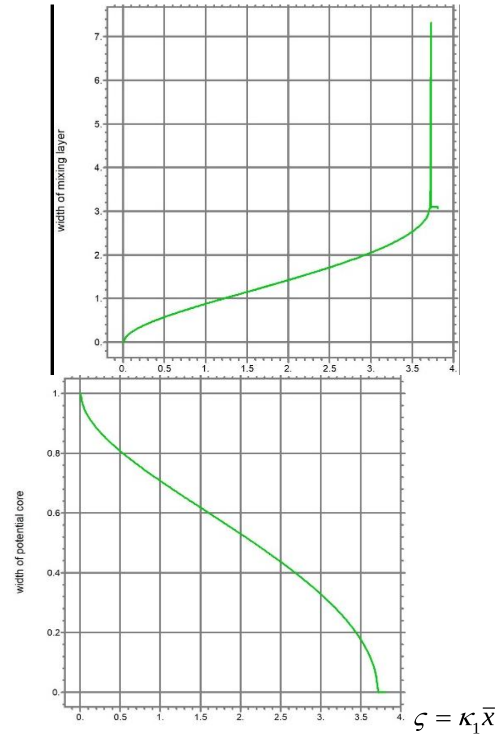

Fig. 14: Functionsδ(ζ),y0(ζ) byi0=0.235,=5.0

Source: created by the authors κ_{21}

The described method, demonstrated in several variants, allows obtaining detailed characteristics of mixing separately by phases. This serves as the basis for accurate calculations of heat and mass transfer in turbulent two-phase jets, which are impossible or much more difficult to do by other methods. A program was created in the FLEX PDE platform for the above calculations.

Initially, the method was developed for mixing liquids with a density ratio from 0.3 to 8.0. It was experimentally confirmed using a specially created two-phase microsensor [26]. We developed the method and completely removed the restrictions on the density ratio. New confirmation was made on experimental data from modelling severe accidents at nuclear power plants with the modelling melts [27] (Table 1):

Table 1. Experimental data: r_0=0.3 mm, $\mu_1 = 2 \cdot 10^{-5} N \cdot s/m^2$, $\rho_1 = 2.1 \quad kg/m^3$

Cases	κ_1		$u_{0,l}$ (m/sec)		$\rho_{2,1}$		$\mu_{2,1}$ (20^oC)	
	water	paraf.	water	paraf.	water	paraf.	water	paraf.
(a)	0.008	0.016	0.23	0.29	476	419	4.16	271
(b)	0.031	0.007	0.29	0.59	476	419	4.16	271
(c)	0.058	0.014	0.59	0.17	476	419	4.16	271
(d)	0.014	0.009	0.29	0.29	476	419	4.16	271
(e)	0.008	0.014	0.59	0.47	476	419	4.16	271
(f)	0.012	0.011	0.29	0.59	476	419	4.16	271
(g)	0.012	0.011	0.59	0.77	476	419	4.16	271
(h)	-	0.012	-	1.01	-	419	-	271

Source: [27]

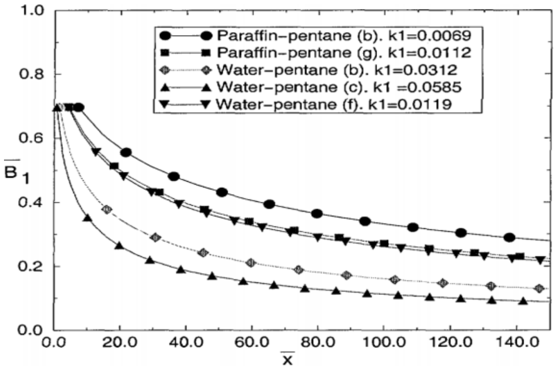

Fig. 15: Function-indicator B1 for different cases
Source: [27]

In these experiments with high-temperature melts, no two-phase sensors were available, but calculation by the described two-phase method presented precise results of diverse averaged characteristics as clearly observed from the presented data. The latter was extremely important for estimation of the melt cooling during potential severe accidents at the nuclear power plants.

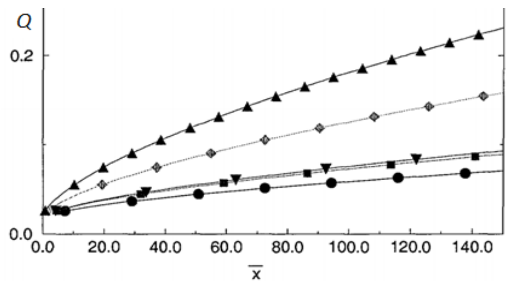

Fig. 16: Tendency for Q for different flow cases
Source: [27].

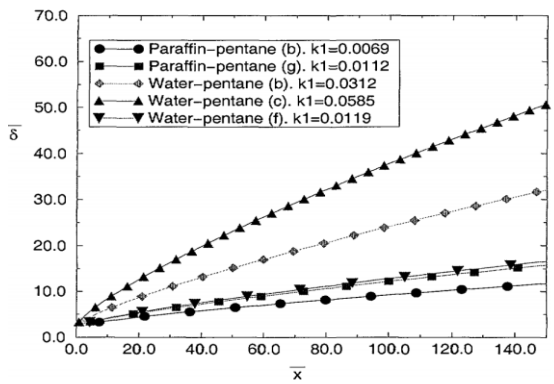

Fig. 17: The width of the mixing zone for flow cases
Source: [27].

5 Conclusion

Based on simulation for Al Nano powder and micro powder and their jet flow with water, one can consider the optimal regime for the mixture of the powder with liquids and mixing of different liquids.

The nature of the initial part of the jet, which retains a pronounced potential core with a constant velocity, is as follows. The main changes in parameters occur in the mixing zone. The effect of the density difference is such that the reduced density of the pool (compared to the liquid in the nozzle) leads to a more intense expansion of the jet and a slower attenuation of the axial velocity. This is manifested in an increase in the width of the jet and a steeper velocity gradient in the cross sections. The velocity and pressure distributions obtained in computer simulation demonstrate a typical picture of a free turbulent jet: a maximum velocity on the axis, its gradual decrease along the axis, and the alignment of the profiles in the radial direction.

The zone of increased pressure gradients is localized near the nozzle exit. The selected mathematical model of multiphase flows [26] and the obtained system of equations and approximations of velocities and indicator functions provide a physically justified description of the process. The obtained numerical results are qualitatively (and, if data are available, quantitatively) consistent with theoretical concepts and literature data for similar two-phase turbulent jet flow regimes.

References:

[1] ASTM International/International Standard, 2015, "ISO/ASTM 52900:2015 - Additive Manufacturing -General Principles - Terminology."

[2] Du, W., Ren, X., Pei, Z., and Ma, C., 2020, "Ceramic Binder Jetting Additive Manufacturing: A Literature Review on Density," Journal of Manufacturing Science and Engineering, 142(4), pp. 1–66. https://doi.org/10.1115/1.4046248.

[3] Li, M., Du, W., Elwany, A., Pei, Z., and Ma, C., 2020, "Metal Binder Jetting Additive Manufacturing: A Literature Review," Journal of Manufacturing Science and Engineering, 142(9), pp. 1–45. doi: 10.1115/1.4047430.

[4] Qian, C., and Sun, J., 2013, "Fabrication of the Porous Hydroxyapatite Implant by 3D Printing," Journal of Ceramic Processing Research, 14(4), pp. 513–516.

[5] Tarafder, S., Davies, N. M., Bandyopadhyay, A., and Bose, S., 2013, "3D Printed Tricalcium Phosphate Bone Tissue Engineering Scaffolds: Effect of SrO and MgO Doping on in Vivo Osteogenesis in a Rat Distal Femoral Defect Model,"

Biomaterials Science, 1(12), pp. 1250–1259. doi: 10.1039/C3BM60132C.

[6] Tarafder, S., Dernell, W. S., Bandyopadhyay, A., and Bose, S., 2015, “SrO- and MgO-Doped Microwave Sintered 3D Printed Tricalcium Phosphate Scaffolds: Mechanical Properties and in Vivo Osteogenesis in a Rabbit Model,” Journal of Biomedical Materials Research - Part B Applied Biomaterials, 103(3), p. 679–690. https://doi.org/10.1002/jbm.b.33239.

[7] Miao, G., Du, W., Moghadasi, M., Pei, Z., and Ma, C., 2020, “Ceramic Binder Jetting Additive Manufacturing: Effects of Granulation on Properties of Feedstock Powder and Printed and Sintered Parts, ”Additive Manufacturing, 36, p. 101542. doi: 10.1016/j.addma.2020.101542.

[8] Bai, Y., Wagner, G., and Williams, C. B., 2015, “Effect of Bimodal Powder Mixture on Powder Packing Density and Sintered Density in Binder Jetting of Metals,” International Solid Freeform Fabrication Symposium, Austin, TX, p. 758–771.

[9] Butscher, A., Bohner, M., Roth, C., Ernstberger, A., Heuberger, R., Doebelin, N., Rudolf Von Rohr, P., and Müller, R., 2012, “Printability of Calcium Phosphate Powders for Three-Dimensional Printing of Tissue Engineering Scaffolds,” Acta Biomaterialia, 8(1), p. 373–385. doi: 10.1016/j.actbio.2011.08.027.

[10] Zocca, A., Gomes, C. M., Bernardo, E., Muller, R., Gunster, J., and Colombo, P., 2013, “LAS GlassCeramic Scaffolds by Three-Dimensional Printing,” Journal of the European Ceramic Society, 33(9), p. 1525–1533. https://doi.org/10.1016/j.jeurceramsoc.2012.12.012.

[11] Lanzetta, M., and Sachs, E., 2001, “The Line Formation with Alumina Powders in Drop on Demand Three Dimensional Printing,”1st Int. Seminar on Progress in Innovative Manufacturing Engineering, Sestri Levante, p. 197–204.

[12] Sun, C., Tian, X., Wang, L., Liu, Y., Wirth, C.M., Günster, J., Li, D., Jin, Z., 2017, “Effect of Particle Size Gradation on the Performance of Glass-Ceramic 3D Printing Process,” Ceramics International, 43(1), p. 578–584. doi: 10.1016/j.ceramint.2016.09.197.

[13] Du, W., Ren, X., Chen, Y., Ma, C., Radovic, M., and Pei, Z., 2018, “Model Guided Mixing of Ceramic Powders with Graded Particle Sizes in Binder Jetting Additive Manufacturing,” ASME 2018 13th International Manufacturing Science and Engineering Conference, College Station, TX, pp. 1–9. https://doi.org/10.1115/MSEC2018-6651.

[14] Du, W., Roa, J., Hong, J., Liu, Y., Pei, Z., Ma, C., 2021, “Binder Jetting Additive Manufacturing: Effect of Particle Size Distribution on Density,” Journal of Manufacturing Science and Engineering, 143(9), p. 091002_1–26. doi: 10.1115/1.4050306.

[15] Suwanprateeb, J., Sanngam, R., and Panyathanmaporn, T., 2010, “Influence of Raw Powder Preparation Routes on Properties of Hydroxyapatite Fabricated by 3D Printing Technique,” Materials Science and Engineering C, 30(4), p. 610–617. https://doi.org/10.1016/j.msec.2010.02.014.

[16] Irsen, S. H., Leukers, B., Höckling, C., Tille, C., and Seitz, H., 2006, “Bioceramic Granulates for Use in 3D Printing: Process Engineering Aspects,” Materialwissenschaft und Werkstofftechnik, 37(6), pp. 533–537.

[17] Gildenhaar, R., Knabe, C., Gomes, C., Linow, U., Houshmand, A., Berger, G., 2011, “Calcium Alkaline Phosphate Scaffolds for Bone Regeneration 3D-Fabricated by Additive Manufacturing,” Key Engineering Materials, 493, p. 849–854. doi: 10.4028/www.scientific.net/KEM.493-494.849.

[18] Ben, Y., Zhang, L., Wei, S., Zhou, T., Li, Z., Yang, H., Wang, Y., A. Selim, F.A., Wong, C., Chen, H., 2017, “PVB Modified Spherical Granules of β-TCP by Spray Drying for 3D Ceramic Printing,” Journal of Alloys and Compounds, 721, p. 312–319. doi: 10.1016/j.jallcom.2017.06.022.

[19] Seitz, H., Deisinger, U., Leukers, B., Detsch, R., Ziegler, G., 2009, “Different Calcium Phosphate Granules for 3-D Printing of Bone Tissue Engineering Scaffolds,” Advanced Engineering Materials, 11(5), p. 41–46. doi: 10.1002/adem.200800334.

[20] Cox, S.C., Thornby, J.A., Gibbons, G.J., Williams, M.A., Mallick, K.K., 2015, “3D Printing of Porous Hydroxyapatite Scaffolds Intended for Use in Bone Tissue Engineering Applications,” Materials Science and Engineering C, 47, p. 237–247. doi: 10.1016/j.msec.2014.11.024.

[21] Chumnanklang, R., Panyathanmaporn, T., Sitthiseripratip, K., and Suwanprateeb, J., 2007, "3D Printing of Hydroxyapatite: Effect of Binder Concentration in Pre-Coated Particle on Part Strength," Materials Science and Engineering C, 27(4), p. 914–921. https://doi.org/10.1016/j.msec.2006.11.004.

[22] Du, W., Miao, G., Liu, L., Pei, Z., and Ma, C., 2019, "Binder Jetting Additive Manufacturing of Ceramics: Feedstock Powder Preparation by Spray Freeze Granulation," ASME 2019 14th International Manufacturing Science and Engineering Conference, Errie, PA, p. 1–6. https://doi.org/10.1115/MSEC2019-2983.

[23] Du, W., Miao, G., Liu, L., Pei, Z., and Ma, C., 2019, "Binder Jetting Additive Manufacturing of Ceramics: Comparison of Flowability and Sinterability between Raw and Granulated Powders," ASME 2019 14th International Manufacturing Science and Engineering Conference, Errie, PA, p. 1–8. doi: 10.1115/MSEC2019-2983.

[24] Ganji, D.D., Mahboobtosi, M., Chari, F.N. Nonlinear radiation in entropy generation MHD flow of penta-hybrid nanofluids: Effects of variable thermal conductivity, viscous dissipation and nonlinear convection// Journal of Radiation Research and Applied Sciences. Vol. 18, Issue 2, June 2025, 101524. https://doi.org/10.1016/j.jrras.2025.101524.

[25] Jalili B., Zar, P.M., Liu, D., Ji, C.-H., Jalili, P., Abdelmohimen, M.A.H., Ganji, D.D. Thermal study of MHD hybrid nanofluids confined between two parallel sheets: Shape factors analysis// Case Studies in Thermal Engineering. Volume 63, November 2024, 105229: https://doi.org/10.1016/j.csite.2024.105229.

[26] *(text in Ukrainian)* Nakorchevski A.I., Basok B.I. Hydrodynamics and heat transfer in heterogeneous systems and devices of pulsating type. Kyiv: Naukova Dumka, 2001, p.348.

[27] Nakorchevskyi A.I. Heterogeneous turbulent jets. Kyiv: Naukova Dumka, 1980, p.142.

[28] Kazachkov Ivan. Turbulent Two-Phase Jets of Mutually Immiscible Liquids: Mixing and Heat Transfer. Cambridge Scholars Publishing. 2025, p.219.

Contribution of Individual Authors to the Creation of a Scientific Article (Ghostwriting Policy)

Ivan Kazachkov contributed in the present research, at all stages from the formulation of the problem to the final findings and solution.

Sources of Funding for Research Presented in a Scientific Article or Scientific Article Itself

Grant from the Swedish Strategic Research Foundation in 2022-2023.

Conflict of Interest

The author has no conflicts of interest to declare that are relevant to the content of this article.